Full title: Eye-specific synaptic clustering through activity-dependent stabilization and punishment mechanisms in the developing visual system

Short title: Activity-dependent synaptic clustering underlies eye-specific competition

Author list: Chenghang Zhang[1] and Colenso M. Speer[1,*]

Author Affiliations: [1] Department of Biology, University of Maryland, College Park, Maryland, USA. 20742.

[*]Corresponding author

E-mail: cspeer@umd.edu (CS)

Abstract

Co-active synaptic connections are often spatially clustered to enable local dendritic computations underlying learning, memory, and basic sensory processing. In the mammalian visual system, retinal ganglion cell (RGC) axons converge to form clustered synaptic inputs for local signal integration in the dorsal lateral geniculate nucleus (dLGN) of the thalamus. Retinogeniculate synapse clustering is promoted by visual experience after eye-opening, but the earliest events in cluster formation and potential regulation by spontaneous retinal wave activity prior to visual experience are unknown. Here, using volumetric super-resolution single-molecule localization microscopy together with eye-specific labeling of developing retinogeniculate synapses in the mouse, we show that synaptic clustering is eye-specific and activity-dependent during the first postnatal week. We identified a subset of complex retinogeniculate synapses with larger presynaptic vesicle pools and multiple active zones that simultaneously promote the clustering of like-eye synapses (synaptic stabilization) and prohibit synapse clustering from the opposite eye (synaptic punishment). In mutant mice with disrupted spontaneous retinal wave activity, complex synapses form, but fail to drive eye-specific synaptic clustering and punishment seen in controls. These results highlight a role for spontaneous retinal activity in regulating eye-specific stabilization and punishment signals contributing to synaptic clustering in circuits essential for visual perception and behavior.

Introduction

A hallmark of neuronal computation is the formation of spatially clustered synaptic inputs to facilitate local computations within individual dendrites (1-3). Through linear and non-linear signal integration mechanisms, synaptic clusters play critical computational roles in learning, memory, and sensory processing underlying cognition and behavior (4-7). During circuit development, the formation of synaptic clusters is regulated by both spontaneous and sensory-driven neural activity that helps to stabilize or eliminate individual synapses to establish mature connectivity patterns (5, 6, 8).

A model example of activity-dependent synaptic cluster formation is the refinement of retinal inputs to the dorsal lateral geniculate nucleus (dLGN) of the thalamus (9). Electron microscopy (EM) reconstructions of the mouse dLGN reveal the convergence of retinal ganglion cell (RGC) inputs to form “complex” synaptic clusters known as glomeruli (10-13). Each individual glomerulus contains multiple RGC axon terminal boutons formed onto a dendritic branch of a dLGN relay neuron. Individual bouton structures vary from small terminals with a single active zone (AZ) to large and/or perforated synapses containing multiple AZs (10-13). These ultrastructural observations are supported by additional experimental results from transsynaptic (14) and Brainbow-based RGC labeling (11, 13), optogenetic stimulation of RGC axons (15, 16), and calcium imaging of retinogeniculate boutons (17) confirming the clustering of RGC inputs to relay neuron dendrites in the dLGN. Because individual glomeruli often receive inputs from multiple RGCs encoding either similar or distinct visual features (17), the proper developmental wiring of RGC bouton clusters is critical for local dendritic integration functions that drive visual spike responses in the adult brain.

Previous studies have shown that synaptic cluster development in neural circuits depends upon spatiotemporally correlated synaptic activity that induces local biochemical and mechanical signaling mechanisms to regulate synaptogenesis, pruning, and plasticity (6, 18). In the developing retinogeniculate system, there are two sources of correlated activity that could contribute to synaptic clustering: 1) visual experience that drives topographic activation of neighboring RGCs and 2) spontaneous retinal wave activity that correlates burst firing of neighboring RGCs prior to eye-opening. Consistent with experience-dependent plasticity, retinogeniculate bouton clustering increases after eye-opening (10, 13, 19) and visual deprivation reduces clustering (19). However, these experience-dependent changes occur long after the spontaneous activity-dependent segregation of eye-specific retinogeniculate axons prior to eye-opening (20-22). Before photoreceptor-mediated visual onset, retinal waves generate spatiotemporal correlations in RGC burst activity that are predicted to facilitate Hebbian strengthening of co-active synapses (Butts et al., 2007) and promote eye-specific synaptic clustering. Whether retinogeniculate synapse clustering begins prior to eye-opening and is regulated by spontaneous retinal activity is unknown.

To address this question, we used volumetric super-resolution microscopy together with anterograde tract tracing and immunohistochemical synaptic protein labeling to investigate the development of clustered eye-specific synapses in the dLGN prior to the onset of photoreceptor-mediated visual experience. During the first postnatal week, we identified a subpopulation of retinogeniculate synapses from both eyes-of-origin that contained larger presynaptic vesicle pools and multiple active zones (AZs). These “complex” synapses acted as loci for the clustering of synapses from the same eye (synaptic stabilization). At the same time, complex synapses of opposite eyes-of-origin showed a distance-dependent interaction that reduced synaptic clustering in an eye-specific manner during retinogeniculate competition (synaptic punishment). These patterns of synaptic stabilization and punishment were absent in a genetic mutant mouse line with disrupted stage II cholinergic retinal waves and abnormal eye-specific segregation. These results demonstrate that spontaneous retinal activity regulates retinogeniculate clustering prior to eye-opening and offer further support for the existence of non-cell-autonomous synaptic stabilization and punishment signals underlying eye-specific competition in the developing visual system.

Results

A unique set of complex synapses shows eye-specific differences during retinogeniculate segregation

To look for evidence of synaptic clustering during eye-specific segregation, we collected super-resolution imaging data in the dLGN of wild-type (WT) mice at three postnatal time points (P2, P4, and P8) (Fig 1A). We labeled eye-specific synapses by monocular injection of Alexa Fluor-conjugated cholera toxin subunit B tracer (CTB) together with immunostaining for presynaptic Bassoon, postsynaptic Homer1, and presynaptic vesicular glutamate transporter 2 (VGluT2) proteins (23). Using volumetric STochastic Optical Reconstruction Microscopy (STORM) (24), we collected separate image volumes (~45K μm^3 each) from three biological replicates at each developmental time point. To determine whether spontaneous retinal activity impacts synaptic clustering across the same time period, we performed identical experiments in a knockout mouse line lacking the beta 2 subunit of the nicotinic acetylcholine receptor (β2KO), which disrupts spontaneous cholinergic retinal wave activity, eye-specific axonal segregation, and retinogeniculate synapse development (20, 23, 25-33). Because eye-specific segregation is incomplete until P8 in the mouse, we limited our analysis to the future contralateral eye-specific region of the dLGN, which is reliably identified across all stages of postnatal development (Fig 1A, see also Materials and methods).

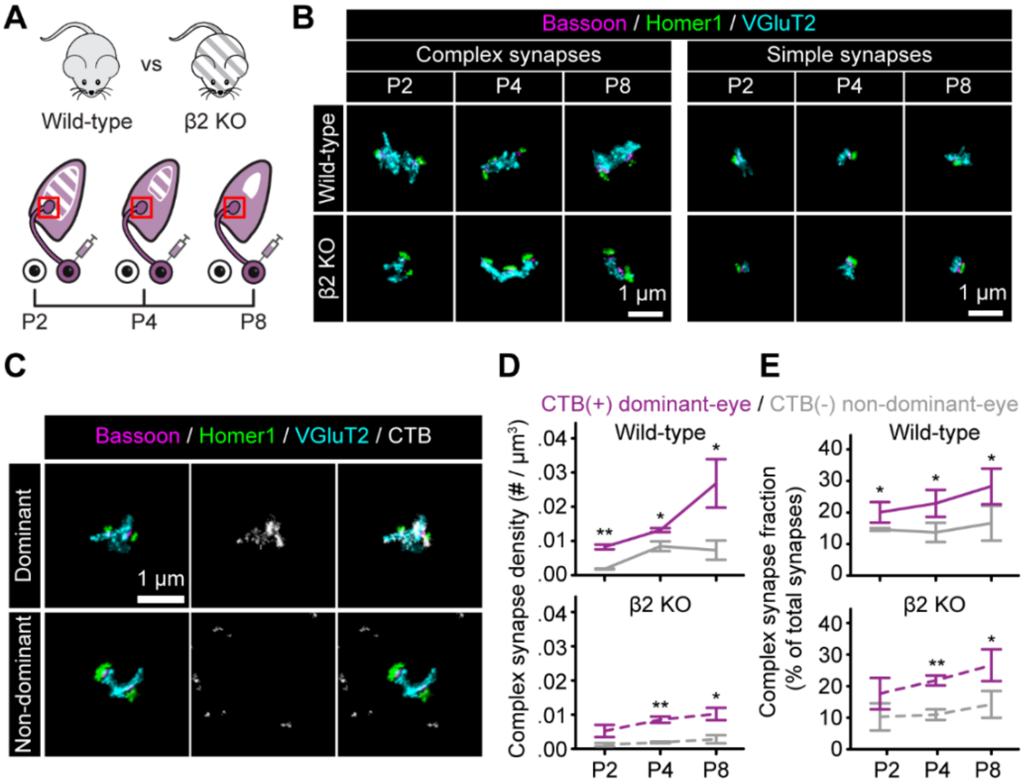

Fig 1. A unique set of complex synapses shows eye-specific differences during retinogeniculate segregation. (A) Experimental design: CTB-Alexa 488 was injected into the right eye of wild-type (WT) and β2KO mice. Tissue was collected from the left dLGN at P2, P4, and P8. The red squares indicate the STORM imaging regions. (B) Representative complex (left panels) and simple synapses (right panels) in WT (top panels) and β2KO mice (bottom panels) at each age. (C) Representative CTB(+) dominant-eye (top panels) and CTB(-) non-dominant-eye (bottom panels) complex synapses in a WT P8 sample, showing synaptic (left panels), CTB (middle panels), and merged immunolabels (right panels). (D) Eye-specific complex synapse density across development in WT (top panel) and β2KO mice (bottom panel). (E) Eye-specific complex synapse fraction across development in WT (top panel) and β2KO mice (bottom panel). In (D) and (E), error bars represent means ± SEMs. Statistical significance between CTB(+) and CTB(-) synapse measurements was assessed using one-way ANOVA. *: $p<0.05$, **: $p<0.01$. N=3 biological replicates for each age/genotype.

Across our dataset collected from different ages and genotypes, the enhanced resolution of STORM images revealed distinct subtypes of retinogeniculate synapses (S1A Fig). These included "complex" synapses characterized by the presence of multiple (2-4) Bassoon(+) active zones (AZs) and greater VGluT2 signal, as well as "simple" retinogeniculate synapses that were smaller and contained a single AZ (Fig 1B and S1A Fig). To determine the eye-of-origin for each retinogeniculate synapse, we measured the colocalization of CTB signal with VGluT2 (Fig 1C). By imaging in the contralateral eye-specific region relative to the CTB-injected eye, we defined CTB(+) VGluT2 clusters as "dominant-eye" synapses originating from the contralateral eye. Conversely, CTB(-) VGluT2 clusters were classified as "non-dominant eye" synapses originating from the ipsilateral eye (Fig 1C). Our previous work using binocular CTB control injections confirmed the high efficiency of retinogeniculate synapse labeling by anterograde tracing, thereby enabling accurate assignment of eye-specific synapses in the mouse brain (23).

After assigning eye-of-origin to all retinogeniculate synapses, we measured the density of complex and simple synapses from both eyes over development. In WT mice, the density of CTB(+) dominant-eye complex synapses increased progressively from P2 to P8 (Fig 1D, upper panel). In contrast, the density of CTB(-) non-dominant-eye complex synapses increased from P2 to P4 and then decreased at P8 (Fig 1D, upper panel). The density of simple synapses followed the same pattern (S1B Fig, upper panel) consistent with the overall refinement of eye-specific synapses (23). In β2KO mice, the density of both complex (Fig 1D, lower panel) and simple eye-specific synapses (S1B Fig, lower panel) was reduced relative to controls at P4 and P8.

To further investigate complex synapse maturation, we measured the fraction of complex synapses relative to the total synapse number over development. In WT mice, the total fraction of dominant-eye complex synapses increased from ~20% at P2 to ~29% at P8 while non-dominant-eye complex synapses remained constant between ~14-17% across the same period (Fig 1E, upper panel). A similar pattern of eye-specific complex synapse maturation was found in β2KO mice (Fig 1E, lower panel), showing that relative proportions of complex versus simple synapses appeared normal despite an overall reduction in total synapse density when spontaneous retinal activity was disrupted (23).

Complex synapses undergo eye-specific vesicle pool maturation

Each complex synapse could represent an individual, larger RGC bouton with multiple active zones, or, alternatively, several clustered simple RGC boutons originating from one or more presynaptic RGC axons (10, 12, 13). To distinguish these possibilities, we compared the developmental changes in VGluT2 volume and active zone number for complex versus simple synapses. In WT mice, both complex (Fig 2A, left panel) and simple (Fig 2B, left panel) synapses showed developmental increases and eye-specific differences in presynaptic VGluT2 volume. In WT complex synapses at P4, the median dominant-eye VGluT2 cluster volumes were 372% larger than non-dominant-eye

VGluT2 clusters (Fig 2A, left panel). In contrast, β2KO mice showed a smaller magnitude difference (110%) between eye-specific complex synapse VGluT2 volume at the same time point (Fig 2A, right panel). In simple synapses at P4, the magnitudes of eye-specific differences in VGluT2 volume were reduced to 135% (WT, Fig 2B, left panel) and 41% (β2KO, Fig 2B, right panel). These results indicate that eye-specific differences in vesicle pool size are more significant for complex synapses versus simple synapses and that the maturation of both synapse types is regulated by spontaneous retinal activity.

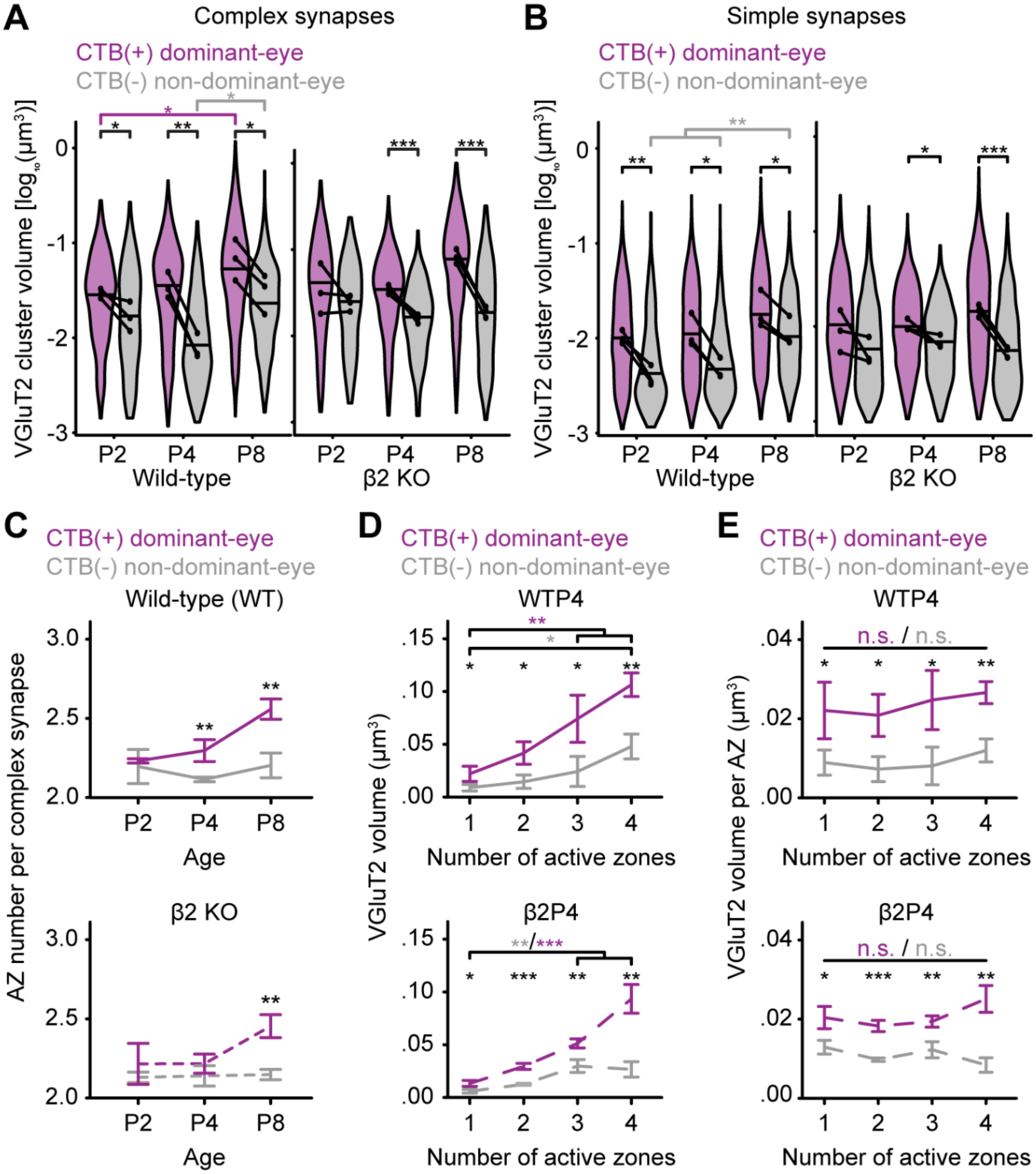
A
Complex synapses
CTB(+) dominant-eye
CTB(-) non-dominant-eye
VGluT2 cluster volume [log₁₀(µm³)]
0
-1
-2
-3
*
*
**
*
***
***
P2
P4
P8
Wild-type
P2
P4
P8
β2 KO
B
Simple synapses
CTB(+) dominant-eye
CTB(-) non-dominant-eye
VGluT2 cluster volume [log₁₀(µm³)]
**
**
*
*
*
***
P2
P4
P8
Wild-type
P2
P4
P8
β2 KO
C
CTB(+) dominant-eye
CTB(-) non-dominant-eye
Wild-type (WT)
AZ number per complex synapse
3.0
2.5
2.0
**
**
P2
P4
P8
Age
β2 KO
**
P2
P4
P8
Age
D
CTB(+) dominant-eye
CTB(-) non-dominant-eye
WTP4
VGluT2 volume (µm³)
.15
.10
.05
.00
**
*
*
*
*
**
1
2
3
4
Number of active zones
β2P4
/*
*
***
**
**
1
2
3
4
Number of active zones
E
CTB(+) dominant-eye
CTB(-) non-dominant-eye
WTP4
VGluT2 volume per AZ (µm³)
.04
.02
.00
n.s. / n.s.
*
*
*
**
1
2
3
4
Number of active zones
β2P4
n.s. / n.s.
*
***
**
**
1
2
3
4
Number of active zones

Fig 2. Complex synapses undergo eye-specific vesicle pool maturation. (A) Violin plots showing the distribution of VGluT2 cluster volume for complex synapses in WT and β2KO mice at each age. The black dots represent the median value of each biological replicate (N=3) and the black horizontal lines represent the median value of all synapses. Black lines connect measurements of CTB(+) and CTB(-) populations from the same biological replicate. Statistical significance was determined using a mixed model ANOVA with a post hoc Bonferroni test. Black asterisks indicate eye-specific differences and colored asterisks indicate differences across time points. (B) Violin plots similar to (A) show the distribution of VGluT2 cluster volume for simple synapses in WT and β2KO mice at each age. (C) Average number of active zones (AZs = individual bassoon clusters) per complex synapse in WT (top panel) and β2KO mice (bottom panel). (D) VGluT2 cluster volume as a function of AZ number for all synapses in WT P4 samples (top panel) and β2KO P4 samples (bottom panel). (E) Average VGluT2 cluster volume per AZ for all synapses in WT P4 samples (top panel) and β2KO P4 samples (bottom panel). In (C-E), error bars represent means ± SEMs from N=3 biological replicates. Statistical significance was assessed using one-way ANOVA with a post hoc Tukey's test. Black asterisks indicate eye-specific differences and colored asterisks indicate differences between simple (1 AZ) and complex (>1 AZ) synapses. "n.s." indicates no significance between simple and complex synapses. In all panels, *: $p<0.05$, **: $p<0.01$, ***: $p<0.001$.

We next measured the number of Bassoon clusters in each complex synapse and asked whether the corresponding VGluT2 cluster volume was consistent with a summation of VGluT2 volume from multiple simple synapses. In both WT (Fig 2C, top panel) and β2KO mice (Fig 2C, bottom panel), complex synapses were associated with an average of 2-3 Bassoon clusters in the first postnatal week. The average number of AZs in CTB(+) dominant-eye complex synapses increased from P2-P8, while CTB(-) non-dominant-eye synapses did not add AZs during this period (Fig 2C). For CTB(+) dominant-eye synapses in both WT and β2KO mice, the size of the vesicle pool was positively correlated with the number of AZs (Fig 2D, S2A/B Figs). This correlation was also present in CTB(-) non-dominant-eye synapses, but with a smaller magnitude. Dividing the total presynaptic VGluT2 volume by the AZ number showed that simple and complex synapses had an equivalent presynaptic vesicle volume associated with each AZ (Fig 2E, S2C/D Figs). This suggests that complex synapses in the first postnatal week are comprised of several simple RGC synapses each with similar VGluT2 volume (putative nascent glomeruli). This conclusion is further supported by EM data showing that individual synaptic terminals in the P7 mouse dLGN are commonly associated with a single AZ (10).

Complex synapses are loci for synaptic clustering

Previous studies support the hypothesis that eye-specific competition is achieved through stabilization and strengthening of co-active dominant-eye RGC inputs together with punishment and elimination of non-dominant-eye inputs (34-36). Within this context, complex synapses with multiple presynaptic release sites may drive strong postsynaptic responses and the induction of non-cell-autonomous stabilization and/or elimination signals that regulate synaptic cluster development (37-39). To investigate whether complex synapses contribute to synaptic clustering, we measured the fraction of eye-specific simple synapses located near like-eye complex synapses and compared this to a randomized simple synapse distribution (Fig 3A-C). Simple synapses were considered nearby if their weighted centroids were within 1.5 µm of a complex synapse edge (Fig 3A, S3 Fig). For CTB(+) dominant-eye projections in WT mice, simple synapses showed non-random clustering near complex synapses, which increased progressively over development (Fig 3B, middle panel). In contrast, when searching for CTB(-) non-dominant-eye simple synapses nearby CTB(+) dominant-eye complex synapses, we found no evidence for synaptic clustering (S3A Fig, middle panel). These results indicate that CTB(+) dominant-eye complex synapses stabilize the local formation of like-eye-type simple synapses.

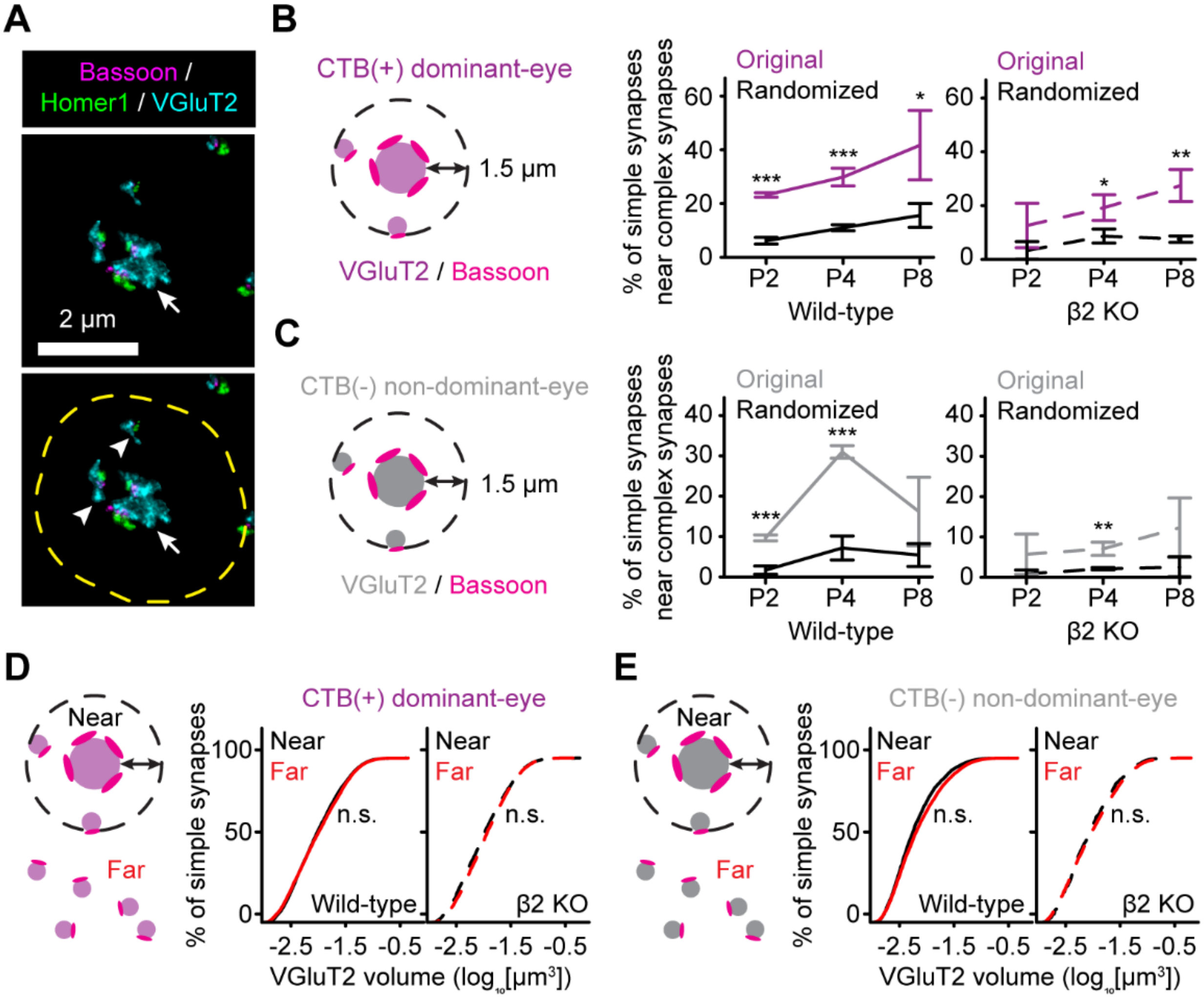

Fig 3. Complex synapses are loci for synaptic clustering. (A) A representative complex synapse in a WT P8 dLGN (arrow) with nearby simple synapses (arrowheads) clustered within 1.5 μm (dashed yellow ring). (B) The fraction of CTB(+) dominant-eye simple synapses near like-eye complex synapses (cartoon) across development in WT (middle panel) and β2KO mice (right panel). Colored lines show the measured distributions and black lines show results of a randomized simple synapse distribution within the sample imaging volume. (C) Same as in (B) showing results for CTB(-) non-dominant-eye simple synapses near like-eye complex synapses. In B/C, a one-way ANOVA was used to test the statistical significance between original and randomized data. Error bars represent means ± SEMs. *: $p<0.05$; **: $p<0.01$; ***: $P<0.001$. (D) Cumulative distribution of simple synapse VGluT2 volume for CTB(+) dominant-eye simple synapses near (<1.5 μm, black lines) or far from (>1.5 μm, red lines) like-eye complex synapses. (E) Same as in (D) showing the cumulative distribution of simple synapse VGluT2 volume for CTB(-) non-dominant-eye simple synapse relative to like-eye complex synapses. The distributions in (D/E) show merged data across all developmental ages. A nonparametric Kolmogorov-Smirnov test was used for statistical analysis. "n.s." indicates no significant difference between near and far simple synapse distributions.

Similarly, for CTB(-) non-dominant-eye complex synapses in WT mice, we observed a significant increase in the clustering of like-eye CTB(-) non-dominant-eye simple synapses nearby from P2 to P4 (Fig 3C, middle panel). Subsequently, the fraction of clustered simple synapses decreased from P4 to P8, reaching a level similar to randomized data (Fig 3C, middle panel). This increase in clustering coincides with ipsilateral RGC axon synaptogenesis (23) and demonstrates that ipsilateral CTB(-) complex synapses promote local synaptogenesis despite being in the future contralateral eye-specific territory. However, after the close of eye-specific competition at P8, clustered CTB(-) simple synapses were eliminated, indicating that CTB(-)

complex synapses failed to stabilize nearby simple synapses during eye-specific competition. This effect was not due to an overall loss of complex synapses as the CTB(-) complex synapse fraction was consistent across the first postnatal week (Fig 1E). Just as we found for CTB(+) dominant-eye complex synapses, CTB(-) non-dominant-eye complex synapses showed no selective stabilization of simple synapses from the opposite eye (S3B Fig, middle panel).

In β2KO mice, CTB(+) dominant-eye complex synapses also stabilized nearby like-eye simple synapses, although the effect size was reduced relative to controls (Fig 3B, right panel). Similarly, CTB(-) non-dominant-eye complex synapses in β2KO mice failed to stabilize like-eye simple synapses to the level seen in controls (Fig 3C, right panel). As we observed in control mice, complex synapses of either eye did not selectively stabilize opposite eye-synapses in β2KO mice (S3A/B Fig, lower panels). Together, these results suggest that while local synapse stabilization mechanisms are at least partially maintained in β2KO mice, defects in spontaneous retinal activity reduce eye-specific synaptic clustering.

Based on our independent findings of eye-specific differences in vesicle pool volume (Fig 2 A/B) and non-random synapse clustering around complex synapses (Fig 3 A-C), we hypothesized that complex synapses might also regulate the vesicle pool size of nearby simple synapses as a mechanism contributing to presynaptic maturation. To test this, we divided the population of simple synapses into two groups: those that were within a 1.5 μm radius of a like-eye complex synapse (‘near’) and those that were at any distance >1.5 µm ('far'). When comparing the vesicle pool volumes between near and far simple synapse groups across all ages and genotypes, we found no significant differences for either dominant-eye or non-dominant-eye simple synapses (Fig 3D/E, displays the data merged for all time points). This result shows that activity-dependent synapse stabilization mechanisms do not impact simple synapse vesicle pool size.

Complex synapses mediate distance-dependent synaptic stabilization and punishment underlying eye-specific competition

RGC axon refinement is a dynamic process involving branch stabilization and elimination based upon the relative activity patterns among neighboring inputs (37, 40). Axonal remodeling is partially regulated by synaptic transmission (41) and the induction of non-cell-autonomous stabilization and punishment signals (38, 39, 42). Although the precise mechanisms of axonal stabilization and punishment are not fully understood, it is likely that non-cell-autonomous signals operate at a local scale through direct cell-cell interactions or diffusible paracrine factors. Based on our observation that CTB(-) non-dominant-eye simple synapses initially cluster around like-eye complex synapses and were eliminated during eye-specific competition (Fig 3C), we hypothesized that CTB(-) synapses may be punished by nearby CTB(+) dominant-eye complex synapses in a distance-dependent manner.

To test this hypothesis, we first examined whether the size of CTB(-) non-dominant-eye complex synapses is affected by their spatial proximity to CTB(+) dominant-eye complex synapses (Fig 4A/B). For each CTB(-) complex synapse, we measured the vesicle pool volume (Fig 4A, P4 data as an example) and AZ number (Fig 4B) as a function of each synapse's distance to the nearest CTB(+) complex synapse. We found no correlation between presynaptic properties and inter-eye complex synapse distances across all ages in both WT mice (Fig 4 A/B, left panels) and β2KO mice (Fig 4A/B, right panels) (P2/P8 data not shown). These findings align with our earlier discovery that simple synapse vesicle pool volume is unaffected by proximity to complex synapses (Fig 3C), suggesting that presynaptic protein organization is not influenced by mechanisms governing synaptic clustering.

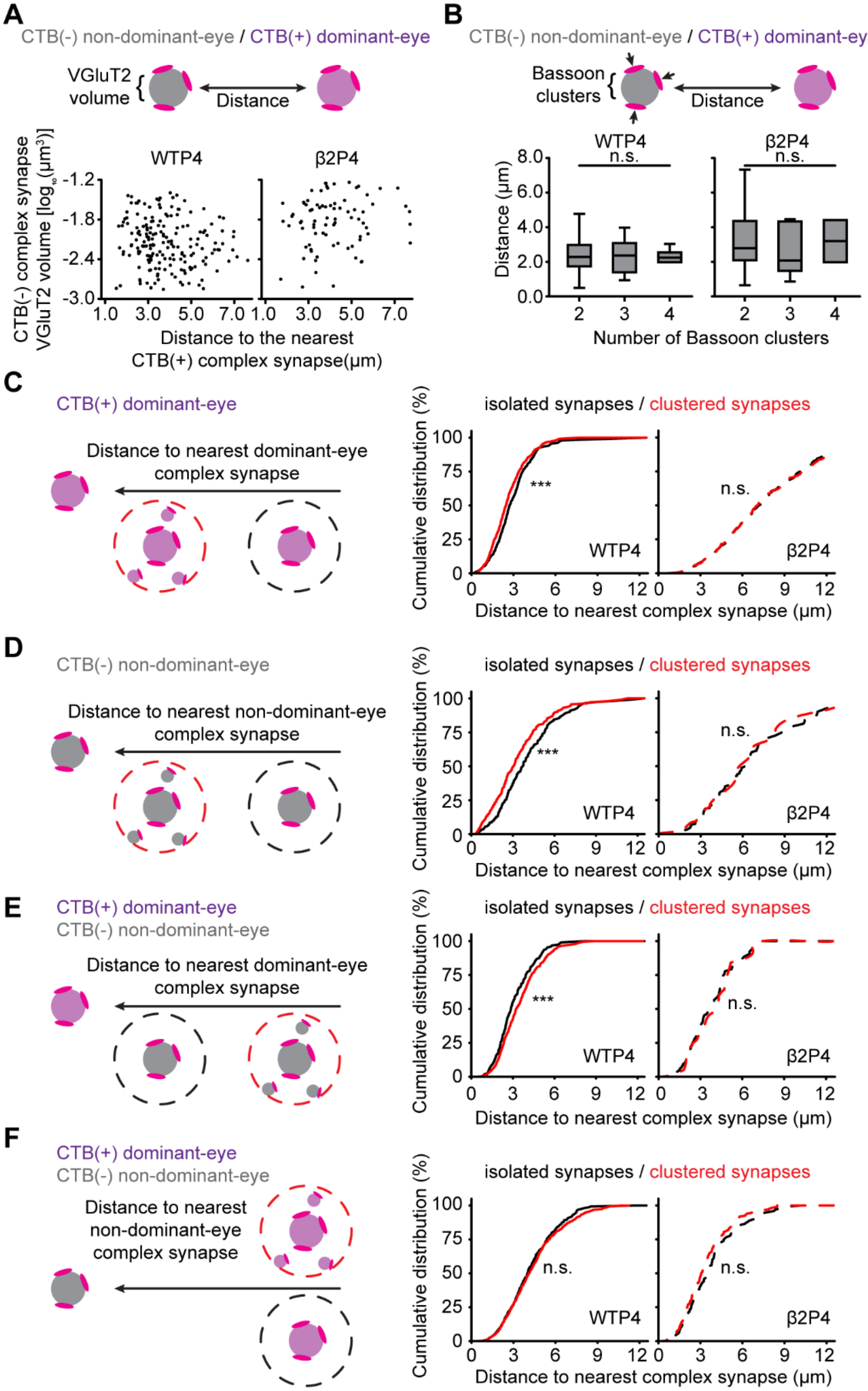
A
CTB(-) non-dominant-eye / CTB(+) dominant-eye
VGluT2 volume
Distance
CTB(-) complex synapse VGluT2 volume [log₁₀(μm³)]
WTP4
β2P4
-1.2
-1.8
-2.4
-3.0
1.0
3.0
5.0
7.0
Distance to the nearest CTB(+) complex synapse(μm)
B
CTB(-) non-dominant-eye / CTB(+) dominant-eye
Bassoon clusters
Distance
WTP4
β2P4
n.s.
n.s.
Distance (μm)
8.0
6.0
4.0
2.0
0.0
2
3
4
Number of Bassoon clusters
C
CTB(+) dominant-eye
Distance to nearest dominant-eye complex synapse
isolated synapses / clustered synapses
Cumulative distribution (%)
100
75
50
25
0
***
n.s.
WTP4
β2P4
0
3
6
9
12
Distance to nearest complex synapse (μm)
D
CTB(-) non-dominant-eye
Distance to nearest non-dominant-eye complex synapse
isolated synapses / clustered synapses
Cumulative distribution (%)
***
n.s.
WTP4
β2P4
Distance to nearest complex synapse (μm)
E
CTB(+) dominant-eye
CTB(-) non-dominant-eye
Distance to nearest dominant-eye complex synapse
isolated synapses / clustered synapses
Cumulative distribution (%)
***
n.s.
WTP4
β2P4
Distance to nearest complex synapse (μm)
F
CTB(+) dominant-eye
CTB(-) non-dominant-eye
Distance to nearest non-dominant-eye complex synapse
isolated synapses / clustered synapses
Cumulative distribution (%)
n.s.
n.s.
WTP4
β2P4
Distance to nearest complex synapse (μm)

Fig 4. Complex synapses mediate distance-dependent synaptic stabilization and punishment underlying eye-specific competition. (A) VGluT2 volume of CTB(-) non-dominant-eye complex synapses relative to their distance to the nearest CTB(+) dominant-eye complex synapse in a WT P4 sample (left panel) and a β2KO P4 sample (right panel). Each black dot represents one synapse. (B) Distributions of distances between CTB(-) non-dominant-eye complex synapses and their nearest CTB(+) dominant-eye complex synapse separated by the number of AZs within each CTB(-) complex synapse in WT P4 samples (left panel) and β2KO P4 samples (right panel). The median value is indicated by the horizontal line within the box, while the box boundaries represent quartile values. The whiskers represent the maximum and minimum values. A mixed model ANOVA was used to perform statistical tests. "n.s." indicates no significance differences. (C) Cumulative distributions of distances between CTB(+) dominant-eye complex synapses and their nearest CTB(+) dominant-eye complex synapse (cartoon) in WT P4 samples (left panel) and β2KO P4 samples (right panel). Red lines indicate clustered complex synapses with nearby (<1.5 μm) simple synapses and black lines indicate isolated complex synapses with no nearby simple synapses. (D) Same presentation as in (C), showing distances between CTB(-) complex synapses. (E) Same presentation as in (C), showing distances between CTB(-) non-dominant-eye complex synapses and their nearest CTB(+) dominant-eye complex synapse (cartoon). (F) Same presentation as in (C), showing distances between CTB(+) dominant-eye complex synapses and the nearest CTB(-) non-dominant-eye complex synapse. For C-F, nonparametric Kolmogorov-Smirnov tests were used for statistical comparisons. "***" indicates p<0.001, while "n.s." indicates no significant differences.

Next, we investigated whether complex synapses influence synaptic clustering around other nearby complex synapses in a distance-dependent manner. For this analysis, we categorized eye-specific complex synapses into two groups: complex synapses with nearby (< 1.5 μm) simple synapses from the same eye (referred to as “clustered”), and complex synapses with no nearby simple synapses (referred to as “isolated”). We then measured the distance between each complex synapse and its closest complex synapses from each eye-of-origin (Fig 4 C-F).

In WT mice at P4, we found that clustered CTB(+) dominant-eye complex synapses were closer to other CTB(+) complex synapses compared to isolated CTB(+) synapses, indicating a synaptic stabilization effect (Fig 4C, left panel). Similarly, clustered CTB(-) non-dominant-eye complex synapses were closer to the nearest CTB(-) complex synapse compared to isolated CTB(-) complex synapses (Fig 4D, left panel). These distance-dependent relationships were not observed when complex synapse positions of the target eye were randomized (S4A/B Fig). These findings indicate that complex synapses from both eyes are more likely to stabilize like-eye-type simple synapses when they are in closer proximity to other complex synapses from the same eye. The stabilization effect of CTB(+) complex synapse clustering persisted until P8 (S4C Fig, left panel). However, by P8, CTB(-) complex synapse stabilization was not observed (S4D Fig, right panel), consistent with synapse elimination and a loss of CTB(-) clustering by this time point (Fig 3C). Furthermore, distance-dependent effects on synaptic clustering at P4 were only observed in WT mice and not in β2KO mice (Fig 4 C/D, right panels; S4E/F Fig, shows P8 β2KO data).

To look for evidence of competitive interactions between synapses from the two eyes, we next measured the distances between clustered and isolated CTB(-) non-dominant eye complex synapses and the closest CTB(+) dominant-eye complex synapse (Fig 4E). In WT mice at P4, we observed that isolated CTB(-) non-dominant-eye complex synapses were closer to the nearest CTB(+) dominant-eye complex synapse compared to clustered CTB(-) synapses (Fig 4E, left panel), consistent with an opposite-eye punishment signal. Similar to our findings on synaptic stabilization, this punishment effect was not observed in β2KO mice (Fig 4E, right panel) or when complex synapse positions of the target eye were randomized (S4A/B Fig).

Lastly, we compared the distances between clustered versus isolated CTB(+) dominant-eye synapses with respect to CTB(-) non-dominant-eye complex synapses and we found no differences in WT mice (Fig 4F, left panel) or β2KO mice (Fig 4F, right panel). This suggests that complex synapses from the non-dominant-eye do not exert a punishment effect on synapses from the dominant-eye (Fig 4F). Together, these results demonstrate that complex synapses contribute to eye-specific competition through activity-dependent stabilization and punishment mechanisms that act locally (within ~6 μm) to regulate synaptic clustering.

Discussion

Relay neurons of the dLGN function as crucial hubs for the integration of RGC inputs within eye-specific synaptic clusters to drive spike output to the primary visual cortex. In this study, we used volumetric super-resolution microscopy together with eye-specific synaptic immunolabeling to show that 1) eye-specific synaptic clustering begins during retinogeniculate refinement prior to eye-opening, 2) synaptic clustering is regulated by a subpopulation of complex synapses with large vesicle pools and multiple AZs, 3) complex synapses regulate clustering through distance-dependent stabilization of like-eye synapses and punishment of opposite-eye synapses, and 4) eye-specific synaptic clustering relies on normal spontaneous retinal wave activity during the first postnatal week. These results advance our understanding of the developmental timeline of retinogeniculate glomerulus development and suggest that spontaneous neural activity regulates synaptic stabilization and punishment signals underlying competitive synaptic refinement in the developing visual system.

Previous anatomical studies have demonstrated the maturation of retinogeniculate glomeruli through the progressive clustering of RGC boutons following eye-opening in mice (10, 13, 19). This process is visual experience-dependent and is partly disrupted by sensory deprivation (late dark-rearing) (19). At maturity, retinogeniculate clusters are primarily eye-specific and contain very few, weak synapses from the non-dominant eye within each eye-specific region (14, 16). Our STORM images reveal that eye-specific synaptic clustering emerges prior to eye-opening, during the period of eye-specific competition regulated by stage II cholinergic retinal waves. This clustering is marked by the development of a subset of complex synapses that contain a greater number of synaptic vesicles and AZs (putative clustered RGC terminal boutons). These synapses differ from simple synapses (isolated RGC terminals) that have fewer vesicles and a single active zone.

Since our STORM images did not include a membrane stain, we were unable to identify the boundaries of individual RGC terminals. Therefore, it remains unclear whether complex synapses represent multiple RGC boutons or single terminals with multiple

AZs. However, several lines of evidence suggest that complex synapses likely consist of two or more small RGC terminals, each with a single AZ. First, we found that the vesicle pool volume in complex synapses is proportional to the number of associated AZs, with each AZ having a comparable vesicle pool size to that of simple synapses. Second, the developmental increase in complex synapse vesicle pool volume matches that of simple synapses. Third, previous electron microscopy (EM) imaging data in the P7 mouse dLGN shows that synaptic profiles are small and mainly associated with a single AZ (10). Larger retinogeniculate terminals containing several AZs are observed later in development after eye-opening (10, 13).

Compared to mature synaptic glomeruli (~ 6 μm diameter), complex synapses formed during the first postnatal week are significantly smaller (~1 μm diameter). This suggests that further aggregation and convergence of RGC inputs are required for the maturation of complex synapses into bona fide glomeruli. Consistent with this, we found that complex synapses acted as local hubs for the clustering of additional like-eye-type simple synapses. The radius of simple synapse clustering around complex synapses was in the range of ~ 3-4 μm, indicating that these clustered simple synapses may serve as the substrate for glomerulus maturation.

In the adult dLGN, bouton clustering facilitates the convergence of RGC inputs representing similar visual features (e.g. direction of motion) and the integration of parallel visual channels carried by unique RGC mosaics (12, 14, 17). Retinal waves drive co-activation of synaptic transmission in boutons from neighboring RGCs, which may support the development of clustered synaptic inputs to relay neurons. Consistent with this, pharmacological and genetic disruptions of cholinergic retinal wave propagation decrease direction selective responses in postsynaptic neurons in the superior colliculus (43). Our STORM images revealed that in β2KO mice with disrupted retinal waves, complex synapses were formed and showed a development increase in vesicle pool volume and AZ number similar to WT mice (Fig 2). However, the clustering of simple synapses around complex synapses was reduced, though not eliminated (Fig 3 B/C), in β2KO mice. Since retinal waves persist in β2KO mice (31-33), a residual level of correlated activity between adjacent RGC synapses may be sufficient to promote synaptic clustering. In the future, it will be of interest to investigate how correlated synaptic activity impacts local clustering using pharmacological or optogenetic manipulations to reduce or enhance RGC correlations in the developing retina (44-47).

While studying the spatial relationships between complex synapses, we observed increased clustering of dominant-eye inputs (stabilization) and decreased clustering of non-dominant-eye inputs (punishment) depending on the distance between eye-specific complex synapses. Synaptic clustering was more likely to occur around complex synapses that were nearby other complex synapses from the same eye (within ~ 6 μm). This finding is consistent with the presence of non-cell-autonomous signals that regulate eye-specific axonal stabilization (37, 38, 42). In addition to mechanisms that stabilize axon branches, eye-specific projections also undergo competitive refinement and axonal retraction mediated by punishment signals. Neurotransmission plays a crucial role in these mechanisms as shown by genetic deletions of VGluT2 or RIM1 proteins from ipsilaterally-projecting RGCs (41, 48). These deletions decrease presynaptic vesicle release and prevent contralateral RGC axon retraction from the ipsilateral eye-specific territory in the dLGN (41, 48). One downstream mediator of synaptic punishment is JAK2 kinase, which is phosphorylated in less active synapses (39). Similar to VGluT2 and RIM1 deletion phenotypes, over-expression of a dominant-negative mutant JAK2 lacking kinase activity prevents axon retraction in transfected RGCs during eye-specific competition (39).

Our super-resolution images show that synapse clustering is less likely to occur around non-dominant-eye complex synapses when they were located nearby dominant-eye complex synapses (a competitive punishment effect). This finding is consistent with previous studies of bulk axonal remodeling and highlights the role of synaptic punishment in axonal refinement phenotypes. In β2KO mice at P4, we did not find evidence of distance-dependent effects on synaptic clustering (either stabilization or punishment), indicating that spontaneous retinal activity regulates eye-specific synaptic clustering mechanisms at a local microcircuit scale (within ~ 6 μm). A possible mechanism underlying this effect is the activity-dependent development of functional presynaptic terminals. We previously found that β2KO mice fail to develop eye-specific differences in vesicle recruitment to the active zone, which are normally present in WT mice as early as P2 (23). This effect is accompanied by an overall reduction in the number of retinogeniculate synapses in the β2KO mouse (23). In the current study, we found that complex synapses show greater eye-specific differences in presynaptic vesicle pool volume compared to simple synapses and that these eye-specific differences are significantly reduced in β2KO mice. Altogether, these results are consistent with a model in which spontaneous retinal activity regulates presynaptic development and vesicle release probability, which is required for the induction of local stabilization and punishment signals that govern eye-specific synapse clustering.

Our results in the developing retinogeniculate system bear similarities to the development of synaptic clusters in other circuits. During the refinement of the neuromuscular junction (NMJ), individual myocytes are initially innervated by multiple motor neuron axons that form intermingled synapses (49, 50). Subsequently, NMJ terminals undergo competitive refinement, where connections from a single motor axon are elaborated and strengthened, while competing axons are eliminated (51, 52). Similar to our findings on eye-specific complex synapse development, competition at the developing NMJ is also dependent on inter-synaptic distance, with motor axons losing connections that are in closer proximity to their competing synapses (49, 50). This process is activity-dependent, and blocking synaptic activity with pharmacological or genetic methods biases competition and leads to elimination of the silenced inputs (53, 54). Interestingly, competing motor axon outputs show differences in presynaptic release probability at early stages of development, suggesting that biases in presynaptic release may underlie competition (55), possibly through the induction of local stabilization and punishment signals (52).

While the molecular mechanisms regulating synaptic competition at the NMJ are not well understood, additional insights have been gained from studies of the developing hippocampus. Synaptic clustering onto hippocampal pyramidal neurons is activity-dependent and is blocked by chronic application of TTX or NMDA-receptor antagonists (56). Activation of NMDA receptors by co-active inputs triggers postsynaptic calcium-induced calcium-release and spreading calcium signals that regulate the maturation of clustered synapses (57). While co-active synapses are strengthened by spontaneous activity, synapses with asynchronous activity undergo synaptic depression, which is blocked by disruptions of proBDNF/P75^{NTR} signaling (58). Similarly, the clustering of co-active inputs is prevented by manipulations of BDNF-TrkB signaling and matrix metalloproteinase 9 (MMP9), a proteinase that converts proBDNF to mature BDNF (59). Together, these findings suggest a model in which postsynaptic activation by co-active inputs drives local spreading intracellular calcium signaling, leading to proBDNF release. Extracellular proBDNF is then cleaved by MMP9 to induce BDNF-TrkB signaling, which stabilizes locally synchronized synapses and promotes cluster maturation (59). At the same time, proBDNF may weaken asynchronous synapses through P75^{NTR} activation (58). Relating these neurotrophic mechanisms to visual system development, a computational model that incorporates BDNF-mediated synaptic refinement suggests that correlations in retinal waves are sufficient to induce local synaptic clustering contributing to orientation selectivity in cortical neurons (60). Supporting a role for correlated spontaneous activity in synaptic refinement for the computation of directional motion, disruptions of retinal wave activity through pharmacological and genetic approaches reduce direction-selective responses in the mouse superior colliculus (43).

Although the molecular mechanisms underlying the clustering of eye-specific retinogeniculate inputs are still unknown, our STORM imaging results provide anatomical support for the existence of local signaling factors that mediate non-cell-autonomous interactions, which underlie both synaptic stabilization and punishment. These factors may induce direct signaling between presynaptic RGC axon terminals or, alternatively, initiate postsynaptic responses that lead to reverse cell-cell signaling or the release of diffusible retrograde factors that stabilize and eliminate synapses based on input timing. JAK2/STAT signaling has been identified as one downstream regulator of synaptic punishment (39), which helps narrow the search for specific upstream induction signals in future experiments. It will also be of special interest to further investigate the eye-specific induction of glial-associated phagocytic signaling pathways that prune weak synapses during eye-specific segregation (61-63).

Materials and methods:

The raw imaging data in this paper were previously reported (23). Materials and methods below are adapted from this work.

Animals

Wild-type C57BL/6J mice used in this study were purchased from the Jackson Laboratory (Stock Number 000664). β2KO mice were a generous gift of Dr. Michael C. Crair (Yale School of Medicine). All experimental procedures were performed in accordance with an animal study protocol approved by the Institutional Animal Care and Use Committee (IACUC) at the University of Maryland. Neonatal male and female mice were used interchangeably for all experiments. Tissue from biological replicates (N=3 animals) was collected for each age (P2/P4/P8) from each genotype (WT and β2KO) (18 animals total). Primers used for genotyping β2KO mice include: forward primer CAGGCGTTATCCACAAAGACAGA; reverse primer TTGAGGGGAGCAGAACAGAATC; mutant reverse primer ACTTGGGTTTGGGCGTGTTGAG (64, 65).

Eye injections

Intraocular eye injections were performed one day before tissue collection. Briefly, mice were anesthetized by inhalant isoflurane and sterile surgical spring scissors were used to gently part the eyelid to expose the corneoscleral junction. A small hole was made in the eye using a sterile 34-gauge needle and ~0.5 µl of cholera toxin subunit B conjugated with Alexa Fluor 488 (CTB-488, ThermoFisher Scientific, Catalogue Number: C34775) diluted in 0.9% sterile saline was intravitreally pressure-injected into the right eye using a pulled-glass micropipette coupled to a Picospritzer (Parker Hannifin).

dLGN tissue preparation

Animals were deeply anesthetized with ketamine/xylazine and transcardially perfused with 5-10 mls of 37°C 0.9% sterile saline followed by 10 mls of room temperature 4% EM Grade paraformaldehyde (PFA, Electron Microscopy Sciences) in 0.9% saline. Brains were embedded in 2.5% agarose and sectioned in the coronal plane at 100 µm using a vibratome. From the full anterior-posterior series of dLGN sections (~6-8 sections) we selected the central two sections for staining in all biological replicates. These sections were morphologically consistent with Figures 134-136 (5.07-5.31 mm) of the postnatal day 6 mouse brain from Paxinos, et al., “Atlas of the developing mouse brain” Academic Press, 2020 (66). Selected sections were postfixed in 4% PFA for 30 minutes at room temperature and then washed for 30-40 minutes in 1X PBS. The dLGN was identified by the presence of CTB-488 signals using a fluorescence dissecting microscope. A circular tissue punch (~500 μm diameter) containing the dLGN was microdissected from each section using a blunt-end needle. A small microknife cut was made at the dorsal edge of the dLGN which, together with the CTB-488 signal, enabled us to identify the dLGN orientation during image acquisition.

Immunohistochemistry

We used a serial-section single-molecule localization imaging approach to prepare samples and collect super-resolution fluorescence imaging volumes as previously described (24). dLGN tissue punches were blocked in 10% normal donkey serum (Jackson ImmunoResearch, Catalogue Number: 017-000-121) with 0.3% Triton X-100 (Sigma-Aldrich Inc.) and 0.02% sodium azide (Sigma-Aldrich Inc.) diluted in 1X PBS for 2-3 hours at room temperature and then incubated in primary antibodies for ~72 hours at 4°C. Primary antibodies used were Rabbit anti-Homer1 (Synaptic Systems, Catalogue Number: 160003, 1:100) to label postsynaptic densities (PSDs), mouse anti-Bassoon (Abcam, Catalogue Number AB82958, 1:100) to label presynaptic active zones (AZs), and guinea pig anti-VGluT2 (Millipore, Catalogue Number AB251-I, 1:100) to label presynaptic vesicles. Following primary antibody incubation, tissues were washed in 1X PBS for 6 x 20 minutes at room temperature and incubated in secondary antibody solution overnight for ~36 hours at 4°C. The secondary antibodies used were donkey anti-rabbit IgG (Jackson ImmunoResearch, Catalogue Number 711-005-152, 1:100) conjugated with Dy749P1 (Dyomics, Catalogue Number 749P1-01) and Alexa Fluor 405 (ThermoFisher, Catalogue Number: A30000), donkey anti-mouse IgG (Jackson ImmunoResearch, Catalogue Number 715-005-150, 1:100) conjugated with Alexa Fluor 647 (ThermoFisher, Catalogue Number: A20006) and Alexa Fluor 405, and donkey anti-guinea pig IgG (Jackson ImmunoResearch, Catalogue Number 706-005-148, 1:100) conjugated with Cy3b (Cytiva, Catalogue Number: PA63101). Tissues were washed 6 x 20 minutes in 1X PBS at room temperature after secondary antibody incubation.

Postfixation, dehydration, and embedding in epoxy resin

Tissue embedding was performed as previously described (24). Tissues were postfixed with 3% PFA + 0.1% GA (Electron Microscopy Sciences) in PBS for 2 hours at room temperature and then washed in 1X PBS for 20 minutes. To plasticize the tissues for ultrasectioning, the tissues were first dehydrated in a graded dilution series of 100% ethanol (50%/70%/90%/100%/100% EtOH) for 15 minutes each at room temperature and then immersed in a series of epoxy resin/100% EtOH exchanges (Electron Microscopy Sciences) with increasing resin concentration (25% resin/75% ethanol; 50% resin/50% ethanol; 75% resin/25% ethanol; 100% resin; 100% resin) for 2 hours each. Tissues were transferred to BEEM capsules (Electron Microscopy Sciences) that were filled with 100% resin and polymerized for 16 hours at 70°C.

Ultrasectioning

Plasticized tissue sections were cut using a Leica UC7 ultramicrotome at 70 nm using a Histo Jumbo diamond knife (DiATOME). Chloroform vapor was used to reduce compression after cutting. For each sample, ~100 sections were collected on a coverslip coated with 0.5% gelatin and 0.05% chromium potassium (Sigma-Aldrich Inc.), dried at 60 degrees for 25 minutes, and protected from light prior to imaging.

Imaging chamber preparation

Coverslips were chemically etched in 10% sodium ethoxide for 5 minutes at room temperature to remove the epoxy resin and expose the dyes to the imaging buffer for optimal photoswitching. Coverslips were then rinsed with ethanol and dH_2O. To create fiducial beads for flat-field and chromatic corrections, we mixed 715/755nm and 540/560nm, carboxylate-modified microspheres (Invitrogen, Catalogue Numbers F8799 and F8809, 1:8 ratio respectively) to create a high-density fiducial marker and then further diluted the mixture at 1:750 with Dulbecco's PBS to create a low-density bead solution. Both high- and low-density bead solutions were spotted on the coverslip (~0.7 ul each) for flat-field and chromatic aberration correction respectively. Excess beads were rinsed away with dH2O for 1-2 minutes. The coverslip was attached to a glass slide with double-sided tape to form an imaging chamber. The chamber was filled with STORM imaging buffer (10% glucose, 17.5μM glucose oxidase, 708nM catalase, 10mM MEA, 10mM NaCl, and 200mM Tris) and sealed with epoxy.

Imaging setup

Imaging was performed using a custom single-molecule super-resolution imaging system. The microscope contained low (4x/10x air) and high (60x 1.4NA oil immersion) magnitude objectives mounted on a commercial frame (Nikon Ti-U) with back optics arranged for oblique incident angle illumination. We used continuous-wave lasers at 488nm (Coherent), 561nm (MPB), 647nm (MPB), and 750nm (MPB) to excite Alexa 488, Cy3B, Alexa 647, and Dy749P1 dyes respectively. A 405 nm cube laser (Coherent) was used to reactivate Dy749P1 and Alexa647 dye photoswitching. The microscope was fitted with a custom pentaband/pentanotch dichroic filter set and a motorized emission filter wheel. The microscope also contained an IR laser-based focus lock system to maintain optimal focus during automatic image acquisition. Images were collected on 640*640-pixel region of an sCMOS camera (ORCA-Flash4.0 V3, Hamamatsu Photonics) with a pixel size of ~155 nm.

Automated image acquisition

Fiducials and tissue sections on the coverslip were imaged using the low magnification objective (4X) to create a mosaic overview of the specimen. Beads/sections were then imaged at high-magnification (60X) to select regions of interest (ROIs) in the Cy3B and Alexa 488 channels. Before final image acquisition, laser intensities and the incident angle were adjusted to optimize photoswitching for STORM imaging and utilize the full dynamic range of the camera for conventional imaging.

Low-density bead images were taken in 16 partially overlapping ROIs. 715/755nm beads were excited using 750 nm light and images were collected through Dy749P1 and Alexa 647 emission filters. 540/560nm beads were excited using a 488 nm laser and images were collected through Alexa 647, Cy3B, and Alexa 488 emission filters. These fiducial images were later used to generate a non-linear warping transform to correct chromatic aberration. Next, ROIs within each tissue section were imaged at conventional (diffraction-limited) resolution in all four-color channels sequentially.

Following conventional image acquisition, a partially overlapping series of 9 images were collected in the high-density bead field for all 4 channels (Dy749P1, Alexa 647, Cy3B, and Alexa 488). These images were later used to perform a flat-field image correction of non-uniform laser illumination across the ROIs. Another round of bead images was taken as described above in a different ROI of the low-density bead field. These images were later used to confirm the stability of chromatic offsets during imaging. All ROIs within physical sections were then imaged by STORM for Dy749P1 and Alexa 647 channels. Images were acquired using a custom progression of increasing 405nm laser intensity to control single-molecule switching. 8000 frames of Dy749P1 channel images were collected (60 Hz imaging) followed by 12000 frames of Alexa 647 channel images (100 Hz). In a second imaging pass, the same ROIs were imaged for Cy3B and Alexa 488 channels, each for 8000 frames (60 Hz).

We imaged the ipsilateral and contralateral ROIs separately in each physical section of the dLGN. For consistency of ROI selection across biological replicates at each age, we identified the dorsal-ventral (DV) axis of the dLGN and selected ROIs within the center (core region) at 2/5 (ipsilateral ROI) and 4/5 (contralateral ROI) of the full DV length.

Image processing

Single-molecule localization was performed using a previously described DAOSTORM algorithm (67) modified for use with sCMOS cameras (68). Molecule lists were rendered as 8-bit images with 15.5 nm pixel size where each molecule is plotted as an intensity distribution with an area reflecting its localization precision. Low-density fiducial images were used for chromatic aberration correction. We localized 715/755 beads in Dy749P1 and Alexa 647 channels, and 540/560 beads in Alexa 647, Cy3B, and Alexa 488 channels. A third-order polynomial transform map was generated by matching the positions of each bead in all channels to the Alexa 647 channel. The average residual error of bead matching was <15 nm for all channels. The transform maps were applied to both 4-color conventional and STORM images. Conventional images were upscaled (by 10X) to match the STORM image size. The method to align serial sections was previously described (24). STORM images were first aligned to their corresponding conventional images by image correlation. To generate an aligned 3D image stack from serial sections, we normalized the intensity of all Alexa 488 images and used these normalized images to generate both rigid and elastic transformation matrices for all four-color channels of both STORM and conventional data. The final image stack was then rotated and cropped to exclude incompletely imaged edge areas. Images of the ipsilateral regions were further cropped according to CTB-488 signals to exclude contralateral areas.

Cell body filter

The aligned STORM images had non-specific labeling of cell bodies in Dy749P1 and Alexa 647 channels corresponding to Homer1 and Bassoon immunolabels. To limit synaptic cluster identification to the neuropil region we identified cell bodies based on their Dy749P1 signal and excluded these regions from further image processing. STORM images were convolved with a Gaussian function (σ=140 nm) and then binarized using the lower threshold of a two-level Otsu threshold method. We located connected components in the thresholded images and generated a mask based on components larger than e^{11} voxels. Because cell body clusters were orders of magnitude larger than synaptic clusters, the cell body filter algorithm was robust to a range of size thresholds. The mask was applied to images of all channels to exclude cell body areas.

Eye-specific synapse identification and quantification

To correct for minor variance in image intensity across physical sections, we normalized the pixel intensity histogram of each section to the average histogram of all sections. Image histograms were rescaled to make full use of the 8-bit range. Using a two-level Otsu threshold method, the conventional images were thresholded into three classes: a low-intensity background, low-intensity signals above the background representing nonsynaptic labeling, and high-intensity signals representing synaptic structures. The conventional images were binarized by the lower two-level Otsu threshold, generating a mask for STORM images to filter out background signals. STORM images were convolved with a Gaussian function (σ= 77.5 nm) and thresholded using the higher two-level Otsu threshold. Following thresholding, connected components were identified in three dimensions using MATLAB 'conncomp' function. A watershedding approach was applied to split large clusters that were improperly connected. Clusters were kept for further analysis only if they contained aligned image information across two or more physical sections. We also removed all edge synapses from our analysis by excluding synapses that did not have blank image data on all adjacent sides.

To distinguish non-specific immunolabeling from true synaptic signals, we quantified two parameters for each cluster: cluster volume and cluster signal density calculated by the ratio of within-cluster pixels with positive signal intensity in the raw STORM images. Two separate populations were identified in 2D histograms plotted from these two parameters. We manually selected the population with higher volumes and signal densities representing synaptic structures. To test the robustness of the manual selection, we performed multiple repeated measurements of the same data and discovered a between-measurement variance of <1% (data not shown).

To identify paired pre- and postsynaptic clusters, we first measured the centroid-centroid distance of each cluster in the Dy749P1 (Homer1) and Alexa 647 (Bassoon) channels to the closest cluster in the other channel. We next quantified the signal intensity of each opposing synaptic channel within a 140 nm shell surrounding each cluster. A 2D histogram was plotted based on the measured centroid-centroid distances and opposing channel signal densities of each cluster. Paired clusters with closely positioned centroids and high intensities of apposed channel signal were identified using the OPTICS algorithm. In total we identified 49,414 synapses from WT samples (3 samples each at P2/P4/P8, 9 total samples) and 33,478 synapses in $\beta2^{-/-}$ mutants (3 samples each at P2/P4/P8, 9 total samples). Retinogeniculate synapses were identified by pairing Bassoon (Alexa 647) clusters with VGluT2 (Cy3B) clusters using the same method as pre/post-synaptic pairing. Synapses from the right eye were identified by pairing VGluT2 clusters with CTB (Alexa 488) clusters. The volume of each cluster reflected the total voxel volume of all connected voxels, and the total signal intensity was a sum of voxel intensity within the volume of the connected voxels.

Complex synapse identification and quantification

To determine whether an eye-specific VGluT2 cluster is a complex synapse or a simple synapse, we measured the number of active zones (defined by individual Bassoon clusters) associated with each VGluT2 cluster in the dataset. A 3D shell was extended 140 nm from the surface voxels of each VGluT2 cluster and any Bassoon clusters that fell within the shell were considered to be associated with the target VGluT2 cluster. The number of active zones (AZs) associated with each VGluT2 cluster was then measured. VGluT2 clusters associated with more than 1 AZ were defined as complex synapses, while those associated with only 1 AZ were defined as simple synapses.

Quantification of complex and simple synapse VGluT2 cluster volume was performed using the "regionprops" function in MATLAB, which provided the voxel size and weighted centroid of each VGluT2 cluster. The search for simple synapses adjacent to complex synapses (synaptic clustering analysis) was conducted using a similar search approach as for associated Bassoon clusters, with expansion shell sizes ranging from 1 µm to 4 µm from the surface voxels of each complex synapse. The main figures in the study utilized an expansion size of 1.5 µm. An eye-specific simple synapse was considered to be near a complex synapse if its weighted centroid fell within the expanded region.

Quantification and Statistical Analysis

Statistical analysis was performed using SPSS. Plots were generated by SPSS or R (ggplot2). Statistical details are presented in the figure legends. For all measurements in this paper, we analyzed N = 3 biological replicates (individual mice) for each genotype (WT and β2KO) at each age (P2, P4, and P8). Cluster densities, synapse AZ number, average VGluT2 cluster volume, and all fraction measurements were presented as mean ± SEM values in line plots and were compared by one-way ANOVA tests with a post-hoc Tukey’s test when there were more than 2 factors. Nonparametric Kolmogorov-Smirnov tests were used in all cumulative histogram comparisons. We used a linear mixed model to compare VGluT2 cluster volumes (Fig 2) and the distance measurements in Fig 4B. For VGluT2 cluster volume comparisons, the age or eye-of-origin was the fixed main factor and biological replicate IDs were nested random factors. In distance measurement comparisons, the complex synapse AZ number was the fixed main factor and biological replicate IDs were nested random factors. Pairwise comparisons among main factor groups were performed by a post-hoc Bonferroni's test. In violin plots, each violin showed the distribution of grouped data from all biological replicates from the same condition. Each black dot represents the median value of each biological replicate and the horizontal black line represents the group median. Black lines connect measurements of CTB(+) and CTB(-) populations from the same biological replicate. Asterisks in all figures indicate statistical significance: *P<0.05, **P<0.01, ***P<0.001.

Acknowledgements:

We thank Dr. Michael C. Crair for generously sharing the β2KO mouse line used in this work.

Author contributions:

Conceptualization, C.Z. and C.M.S.; data curation, C.Z. and C.M.S.; formal analysis, C.Z. and C.M.S.; funding acquisition, C.M.S.; investigation, C.Z. and C.M.S.; methodology, C.Z. and C.M.S.; project administration, C.Z. and C.M.S.; resources, C.Z. and C.M.S.; software, C.Z. and C.M.S.; supervision, C.M.S.; validation, C.Z. and C.M.S.; visualization, C.Z. and C.M.S.; writing – original draft preparation, C.Z. and C.M.S.; writing – review & editing, C.Z. and C.M.S.

References:

1. Rall W. Electrophysiology of a dendritic neuron model. Biophys J. 1962;2(2 Pt 2):145-67.

2. Mel B, editor The Clusteron: Toward a Simple Abstraction for a Complex Neuron1991 1991: Morgan-Kaufmann.

3. Poirazi P, Mel BW. Impact of active dendrites and structural plasticity on the memory capacity of neural tissue. Neuron. 2001;29(3):779-96.

4. Mel BW, Schiller J, Poirazi P. Synaptic plasticity in dendrites: complications and coping strategies. Curr Opin Neurobiol. 2017;43:177-86.

5. Leighton AH, Lohmann C. The Wiring of Developing Sensory Circuits-From Patterned Spontaneous Activity to Synaptic Plasticity Mechanisms. Front Neural Circuits. 2016;10:71.

6. Winnubst J, Lohmann C. Synaptic clustering during development and learning: the why, when, and how. Front Mol Neurosci. 2012;5:70.

7. Kastellakis G, Poirazi P. Synaptic Clustering and Memory Formation. Front Mol Neurosci. 2019;12:300.

8. Kirchner JH, Gjorgjieva J. Emergence of synaptic organization and computation in dendrites. 2022;28(1):21-30.

9. Bickford ME. Synaptic organization of the dorsal lateral geniculate nucleus. Eur J Neurosci. 2019;49(7):938-47.

10. Bickford ME, Slusarczyk A, Dilger EK, Krahe TE, Kucuk C, Guido W. Synaptic development of the mouse dorsal lateral geniculate nucleus. J Comp Neurol. 2010;518(5):622-35.

11. Hammer S, Monavarfeshani A, Lemon T, Su J, Fox MA. Multiple Retinal Axons Converge onto Relay Cells in the Adult Mouse Thalamus. Cell Rep. 2015;12(10):1575-83.

12. Morgan JL, Berger DR, Wetzel AW, Lichtman JW. The Fuzzy Logic of Network Connectivity in Mouse Visual Thalamus. Cell. 2016;165(1):192-206.

13. Monavarfeshani A, Stanton G, Van Name J, Su K, Mills WA, Swilling K, et al. LRRTM1 underlies synaptic convergence in visual thalamus. Elife. 2018;7:e33498.

14. Rompani SB, Mullner FE, Wanner A, Zhang C, Roth CN, Yonehara K, et al. Different Modes of Visual Integration in the Lateral Geniculate Nucleus Revealed by Single-Cell-Initiated Transsynaptic Tracing. Neuron. 2017;93(4):767-76 e6.

15. Litvina EY, Chen C. Functional Convergence at the Retinogeniculate Synapse. Neuron. 2017;96(2):330-8 e5.

16. Bauer J, Weiler S, Fernholz MHP, Laubender D, Scheuss V, Hubener M, et al. Limited functional convergence of eye-specific inputs in the retinogeniculate pathway of the mouse. Neuron. 2021;109(15):2457-68 e12.

17. Liang L, Fratzl A, Goldey G, Ramesh RN, Sugden AU, Morgan JL, et al. A Fine-Scale Functional Logic to Convergence from Retina to Thalamus. Cell. 2018;173(6):1343-55 e24.

18. Pulikkottil VV, Somashekar BP, Bhalla US. Computation, wiring, and plasticity in synaptic clusters. Curr Opin Neurobiol. 2021;70:101-12.

19. Hong YK, Park S, Litvina EY, Morales J, Sanes JR, Chen C. Refinement of the retinogeniculate synapse by bouton clustering. Neuron. 2014;84(2):332-9.

20. Muir-Robinson G, Hwang BJ, Feller MB. Retinogeniculate axons undergo eye-specific segregation in the absence of eye-specific layers. J Neurosci. 2002;22(13):5259-64.

21. Godement P, Salaün J, Imbert M. Prenatal and postnatal development of retinogeniculate and retinocollicular projections in the mouse. J Comp Neurol. 1984;230(4):552-75.

22. Jaubert-Miazza L, Green E, Lo FS, Bui K, Mills J, Guido W. Structural and functional composition of the developing retinogeniculate pathway in the mouse. Vis Neurosci. 2005;22(5):661-76.

23. Zhang C, Yadav S, Speer CM. The synaptic basis of activity-dependent eye-specific competition. Cell Rep. 2023;42(2):112085.

24. Vatan T, Minehart JA, Zhang C, Agarwal V, Yang J, Speer CM. Volumetric super-resolution imaging by serial ultrasectioning and stochastic optical reconstruction microscopy in mouse neural tissue. STAR Protocols. 2021;2(4):100971.

25. Xu HP, Burbridge TJ, Chen MG, Ge X, Zhang Y, Zhou ZJ, et al. Spatial pattern of spontaneous retinal waves instructs retinotopic map refinement more than activity frequency. Dev Neurobiol. 2015;75(6):621-40.

26. Xu HP, Burbridge TJ, Ye M, Chen M, Ge X, Zhou ZJ, et al. Retinal Wave Patterns Are Governed by Mutual Excitation among Starburst Amacrine Cells and Drive the Refinement and Maintenance of Visual Circuits. J Neurosci. 2016;36(13):3871-86.

27. Xu HP, Furman M, Mineur YS, Chen H, King SL, Zenisek D, et al. An instructive role for patterned spontaneous retinal activity in mouse visual map development. Neuron. 2011;70(6):1115-27.

28. Rossi FM, Pizzorusso T, Porciatti V, Marubio LM, Maffei L, Changeux JP. Requirement of the nicotinic acetylcholine receptor beta 2 subunit for the anatomical and functional development of the visual system. Proc Natl Acad Sci U S A. 2001;98(11):6453-8.

29. Grubb MS, Rossi FM, Changeux JP, Thompson ID. Abnormal functional organization in the dorsal lateral geniculate nucleus of mice lacking the beta 2 subunit of the nicotinic acetylcholine receptor. Neuron. 2003;40(6):1161-72.

30. Dhande OS, Hua EW, Guh E, Yeh J, Bhatt S, Zhang Y, et al. Development of single retinofugal axon arbors in normal and beta2 knock-out mice. J Neurosci. 2011;31(9):3384-99.

31. Sun C, Warland DK, Ballesteros JM, van der List D, Chalupa LM. Retinal waves in mice lacking the beta2 subunit of the nicotinic acetylcholine receptor. Proc Natl Acad Sci U S A. 2008;105(36):13638-43.

32. Stafford BK, Sher A, Litke AM, Feldheim DA. Spatial-temporal patterns of retinal waves underlying activity-dependent refinement of retinofugal projections. Neuron. 2009;64(2):200-12.

33. Bansal A, Singer JH, Hwang BJ, Xu W, Beaudet A, Feller MB. Mice lacking specific nicotinic acetylcholine receptor subunits exhibit dramatically altered spontaneous activity patterns and reveal a limited role for retinal waves in forming ON and OFF circuits in the inner retina. J Neurosci. 2000;20(20):7672-81.

34. Assali A, Gaspar P, Rebsam A. Activity dependent mechanisms of visual map formation--from retinal waves to molecular regulators. Semin Cell Dev Biol. 2014;35:136-46.

35. Fassier C, Nicol X. Retinal Axon Interplay for Binocular Mapping. Front Neural Circuits. 2021;15:679440.

36. Faust TE, Gunner G, Schafer DP. Mechanisms governing activity-dependent synaptic pruning in the developing mammalian CNS. Nat Rev Neurosci. 2021;22(11):657-73.

37. Rahman TN, Munz M, Kutsarova E, Bilash OM, Ruthazer ES. Stentian structural plasticity in the developing visual system. Proc Natl Acad Sci U S A. 2020;117(20):10636-8.

38. Louail A, Sierksma MC, Chaffiol A, Baudet S, Assali A, Couvet S, et al. cAMP-Dependent Co-stabilization of Axonal Arbors from Adjacent Developing Neurons. Cell Rep. 2020;33(1):108220.

39. Yasuda M, Nagappan-Chettiar S, Johnson-Venkatesh EM, Umemori H. An activity-dependent determinant of synapse elimination in the mammalian brain. Neuron. 2021;109(8):1333-49 e6.

40. Munz M, Gobert D, Schohl A, Poquérusse J, Podgorski K, Spratt P, et al. Rapid Hebbian axonal remodeling mediated by visual stimulation. Science. 2014;344(6186):904-9.

41. Koch SM, Dela Cruz CG, Hnasko TS, Edwards RH, Huberman AD, Ullian EM. Pathway-specific genetic attenuation of glutamate release alters select features of competition-based visual circuit refinement. Neuron. 2011;71(2):235-42.

42. Kutsarova E, Schohl A, Munz M, Wang A, Zhang YY, Bilash OM, et al. BDNF signaling in correlation-dependent structural plasticity in the developing visual system. PLoS Biol. 2023;21(4):e3002070.

43. Ge X, Zhang K, Gribizis A, Hamodi AS, Sabino AM, Crair MC. Retinal waves prime visual motion detection by simulating future optic flow. Science. 2021;373(6553).

44. Stellwagen D, Shatz CJ. An instructive role for retinal waves in the development of retinogeniculate connectivity. Neuron. 2002;33(3):357-67.

45. Stellwagen D, Shatz CJ, Feller MB. Dynamics of retinal waves are controlled by cyclic AMP. Neuron. 1999;24(3):673-85.

46. Sun C, Speer CM, Wang GY, Chapman B, Chalupa LM. Epibatidine application in vitro blocks retinal waves without silencing all retinal ganglion cell action potentials in developing retina of the mouse and ferret. J Neurophysiol. 2008;100(6):3253-63.

47. Zhang J, Ackman JB, Xu HP, Crair MC. Visual map development depends on the temporal pattern of binocular activity in mice. Nat Neurosci. 2011;15(2):298-307.

48. Assali A, Le Magueresse C, Bennis M, Nicol X, Gaspar P, Rebsam A. RIM1/2 in retinal ganglion cells are required for the refinement of ipsilateral axons and eye-specific segregation. Sci Rep. 2017;7(1):3236.

49. Balice-Gordon RJ, Chua CK, Nelson CC, Lichtman JW. Gradual loss of synaptic cartels precedes axon withdrawal at developing neuromuscular junctions. Neuron. 1993;11(5):801-15.

50. Gan WB, Lichtman JW. Synaptic segregation at the developing neuromuscular junction. Science. 1998;282(5393):1508-11.

51. Wyatt RM, Balice-Gordon RJ. Activity-dependent elimination of neuromuscular synapses. J Neurocytol. 2003;32(5-8):777-94.

52. Sanes JR, Lichtman JW. Development of the vertebrate neuromuscular junction. Annu Rev Neurosci. 1999;22:389-442.

53. Buffelli M, Burgess RW, Feng G, Lobe CG, Lichtman JW, Sanes JR. Genetic evidence that relative synaptic efficacy biases the outcome of synaptic competition. Nature. 2003;424(6947):430-4.

54. Balice-Gordon RJ, Lichtman JW. Long-term synapse loss induced by focal blockade of postsynaptic receptors. Nature. 1994;372(6506):519-24.

55. Kopp DM, Perkel DJ, Balice-Gordon RJ. Disparity in neurotransmitter release probability among competing inputs during neuromuscular synapse elimination. J Neurosci. 2000;20(23):8771-9.

56. Kleindienst T, Winnubst J, Roth-Alpermann C, Bonhoeffer T, Lohmann C. Activity-dependent clustering of functional synaptic inputs on developing hippocampal dendrites. Neuron. 2011;72(6):1012-24.

57. Lee KF, Soares C, Thivierge JP, Beique JC. Correlated Synaptic Inputs Drive Dendritic Calcium Amplification and Cooperative Plasticity during Clustered Synapse Development. Neuron. 2016;89(4):784-99.

58. Winnubst J, Cheyne JE, Niculescu D, Lohmann C. Spontaneous Activity Drives Local Synaptic Plasticity In Vivo. Neuron. 2015;87(2):399-410.

59. Niculescu D, Michaelsen-Preusse K, Guner U, van Dorland R, Wierenga CJ, Lohmann C. A BDNF-Mediated Push-Pull Plasticity Mechanism for Synaptic Clustering. Cell Rep. 2018;24(8):2063-74.

60. Kirchner JH, Gjorgjieva J. Emergence of local and global synaptic organization on cortical dendrites. Nat Commun. 2021;12(1):4005.

61. Chung WS, Clarke LE, Wang GX, Stafford BK, Sher A, Chakraborty C, et al. Astrocytes mediate synapse elimination through MEGF10 and MERTK pathways. Nature. 2013;504(7480):394-400.

62. Schafer DP, Lehrman EK, Kautzman AG, Koyama R, Mardinly AR, Yamasaki R, et al. Microglia sculpt postnatal neural circuits in an activity and complement-dependent manner. Neuron. 2012;74(4):691-705.

63. Stevens B, Allen NJ, Vazquez LE, Howell GR, Christopherson KS, Nouri N, et al. The classical complement cascade mediates CNS synapse elimination. Cell. 2007;131(6):1164-78.

64. Burbridge TJ, Xu HP, Ackman JB, Ge X, Zhang Y, Ye MJ, et al. Visual circuit development requires patterned activity mediated by retinal acetylcholine receptors. Neuron. 2014;84(5):1049-64.

65. Picciotto MR, Zoli M, Lena C, Bessis A, Lallemand Y, Le Novere N, et al. Abnormal avoidance learning in mice lacking functional high-affinity nicotine receptor in the brain. Nature. 1995;374(6517):65-7.

66. Paxinos G. Atlas of the developing mouse brain at E17.5, P0 and P6. 1st ed. Amsterdam ; Boston: Elsevier; 2007. xi, 353 p. p.

67. Babcock H, Sigal YM, Zhuang X. A high-density 3D localization algorithm for stochastic optical reconstruction microscopy. Optical Nanoscopy. 2012;1(6).

68. Babcock HP, Huang F, Speer CM. Correcting Artifacts in Single Molecule Localization Microscopy Analysis Arising from Pixel Quantum Efficiency Differences in sCMOS Cameras. Sci Rep. 2019;9(1):18058.

Supporting information

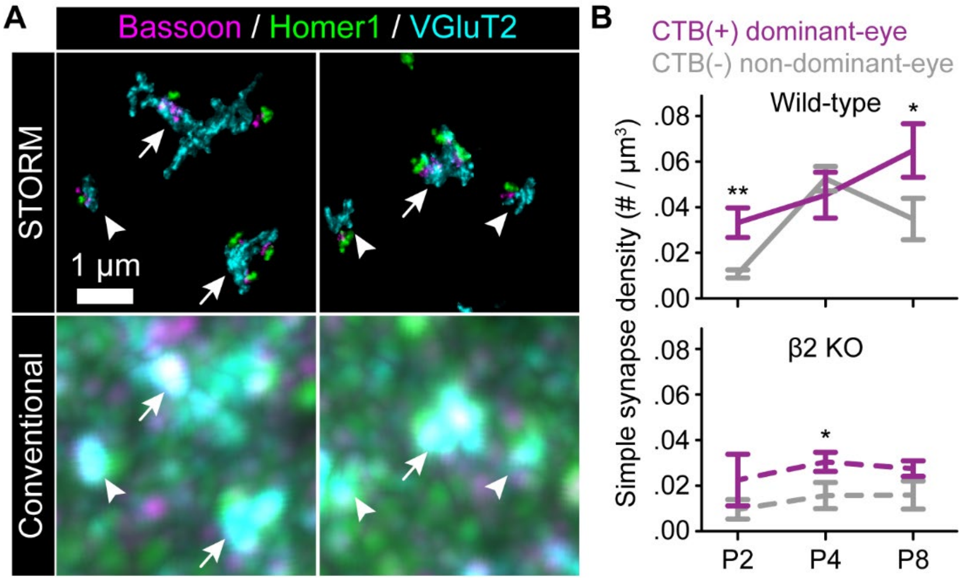

S1 Fig. Eye-specific differences in simple synapse density in the first postnatal week, related to Fig 1. (A) Volumetric STORM imaging enables the differentiation of complex (arrows) versus simple (arrowheads) synapses (top panels), which cannot be distinguished in diffraction-limited conventional images (bottom panels). (B) The density of eye-specific simple synapses across ages in WT (top panel) and β2 KO mice (bottom panel). Error bars represent means ± SEMs (N=3 biological replicates for each age/genotype). Statistical tests were performed using a one-way ANOVA. *: P<0.05. **: p<0.01.

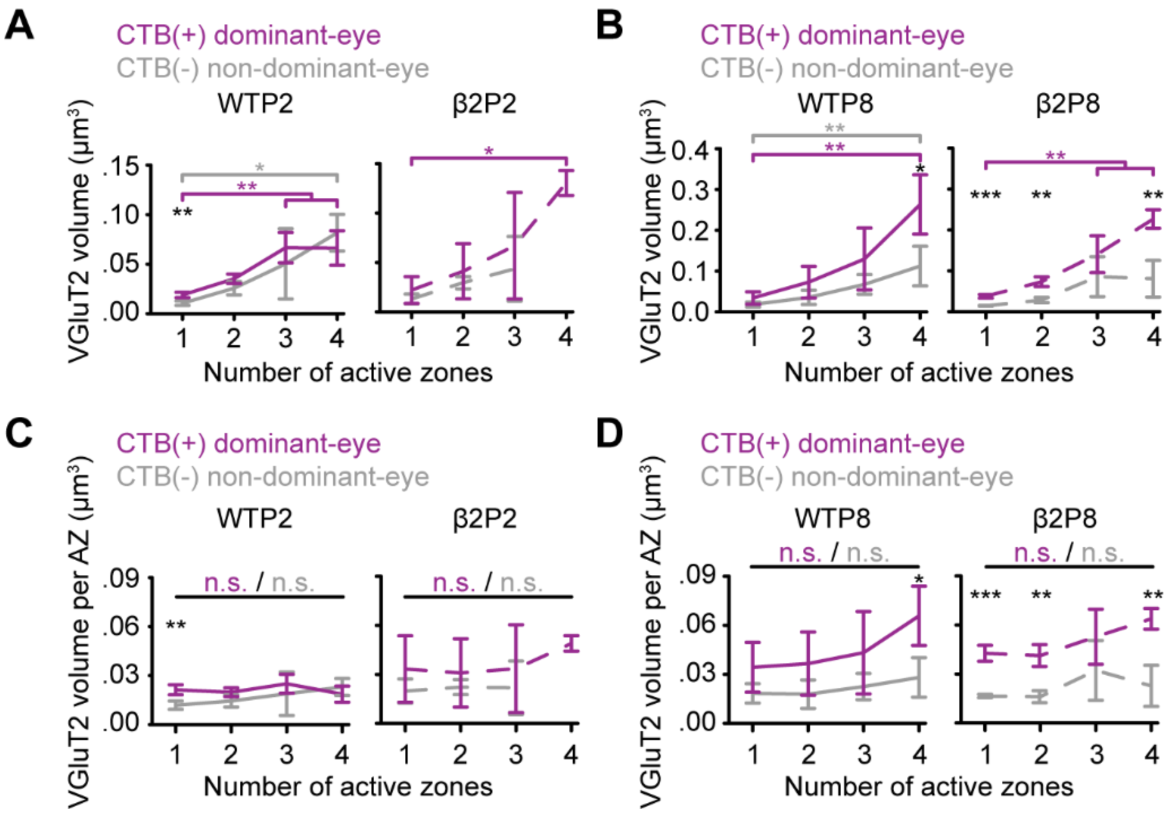

S2 Fig. Complex synapses undergo eye-specific vesicle pool maturation, related to Fig 2. (A-B) VGluT2 cluster volume relative to AZ number for each synapse in WT (left panels) and β2KO mice (right panels) at P2 (A) and P8 (B). Error bars indicate means ± SEMs (N=3 biological replicates for each age and genotype). A one-way ANOVA was used to assess statistical significance between eye-of-origin (black asterisks) and eye-specific synapses with different AZ numbers (colored asterisks). A post hoc Tukey's test was conducted for pairwise comparisons between simple (1 AZ) and complex (>1 AZ) synapses. (C-D) VGluT2 volume per AZ (bassoon cluster) for all synapses in WT (left panels) and β2KO mice (right panels) at P2 (C) and P8 (D). Figure presentation and statistical tests were the same as shown in (A) and (B). In all panels: *: $p<0.05$; **:$p<0.01$; ***:$p<0.001$.

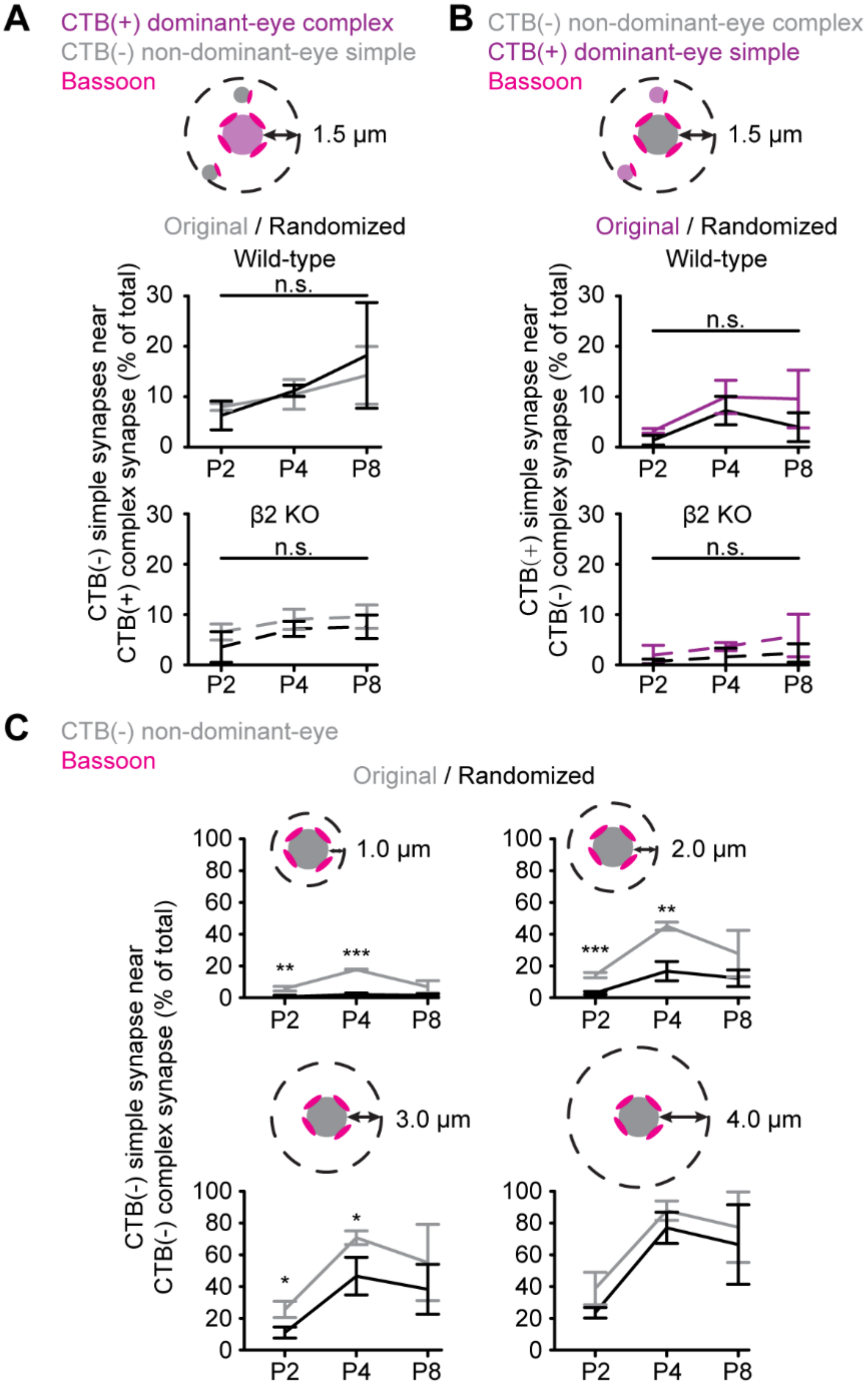

S3 Fig. Complex synapses are loci for synaptic clustering, related to Fig 3. (A) Percentage of CTB(-) non-dominant-eye simple synapses near an opposite-eye complex synapse in WT (top panel) and β2KO mice (bottom panel). (B) Same presentation as in (A), showing percentage of CTB(+) dominant-eye simple synapses near an opposite-eye complex synapse. (C) To further validate our selection of a 1.5 um search radius, we performed additional control measurements with varying local search radii. For complex synapses of both eyes-of-origin, the detection of non-random clustering increased when the search radius was expanded from 1 μm to 2 μm and then decreased as the radius was further expanded to sample the average simple synapse density (3-4 μm) (example with CTB(-) non-dominant-eye synapses). The figure shows the percentage of CTB(-) non-dominant-eye simple synapses near like-type CTB(-) complex synapses across development as a function of increasing distance cutoffs from the surface of complex synapses. Distributions are shown for cutoff distances of 1.0 μm (top left panel), 2.0 μm (top right panel), 3.0 μm (bottom left panel), and 4.0 μm (bottom right panel). For all panels, grey and purple lines represent the original data, and black lines represent the results from a randomized simple synapse distribution. Error bars represent means ± SEMs (N=3 biological replicates for each age and genotype). Statistical tests between original and randomized data were performed using one-way ANOVA. *: $P<0.05$; **: $p<0.01$; ***: $p<0.001$. “n.s.” indicates no significant differences.

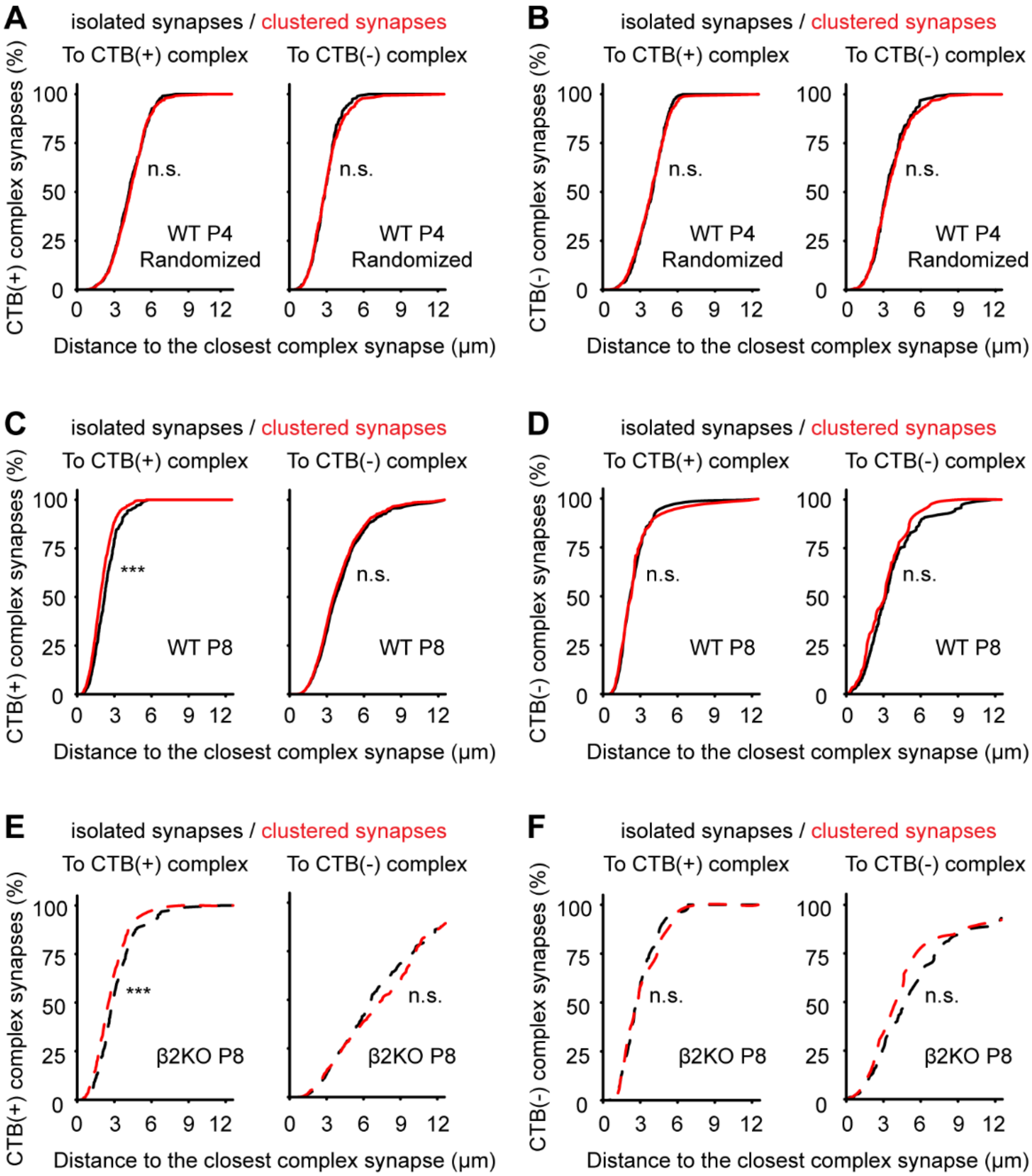

S4 Fig. Complex synapses mediate distance-dependent synaptic stabilization and punishment underlying eye-specific competition, related to Fig. 4. (A) Cumulative histogram of the distances from CTB(+) complex synapses to their nearest CTB(+) (left panel) and CTB(-) (right panel) complex synapse in P4 WT data where simple synapse distributions were randomized. Black lines show distributions for isolated complex synapses with no nearby (<1.5 μm) simple synapses and red lines show distributions for clustered complex synapses with one or more simple synapses nearby. (B) Same presentation as in (A), showing distances from CTB(-) complex synapses to their nearest CTB(+) (left panel) and CTB(-) (right panel) complex synapse in P4 WT randomized data. (C and D) Same presentation as in A/B, showing WT P8 original data. (E and F) Same presentation as in C/D, showing β2KO P8 original data. Nonparametric Kolmogorov-Smirnov tests were used for statistical comparisons (N=3 biological replicates for each condition). ***: $p<0.001$. "n.s." indicates no significant differences.